Optical generation of intense ultrashort magnetic pulses at the nanoscale

2013 New J. Phys. 15 113035

(http://iopscience.iop.org/1367-2630/15/11/113035)

New Journal of Physics
The open access journal for physics

Optical generation of intense ultrashort magnetic pulses at the nanoscale

Anagnostis Tsiatmas[1], **Evangelos Atmatzakis**[1],
Nikitas Papasimakis[1], **Vassili Fedotov**[1], **Boris Luk'yanchuk**[2],
Nikolay I Zheludev[1,3] **and F Javier García de Abajo**[1,4,5,6]

[1] Optoelectronics Research Centre and Centre for Photonic Metamaterials, University of Southampton, Southampton SO17 1BJ, UK
[2] Data Storage Institute, Agency for Science, Technology and Research, Singapore 117608, Singapore
[3] Centre for Disruptive Photonic Technologies, Nanyang Technological University, Singapore 637371, Singapore
[4] ICFO—Institut de Ciencies Fotoniques, Mediterranean Technology Park, 308860 Castelldefels, Barcelona, Spain
[5] ICREA—Institució Catalana de Recerca i Estudis Avançats, 08010 Barcelona, Spain
E-mail: javier.garciadeabajo@icfo.es

New Journal of Physics **15** (2013) 113035 (18pp)
Received 14 June 2013
Published 15 November 2013
Online at http://www.njp.org/
doi:10.1088/1367-2630/15/11/113035

Abstract. Generating, controlling and sensing strong magnetic fields at ever shorter time and length scales is important for both fundamental solid-state physics and technological applications such as magnetic data recording. Here, we propose a scheme for producing strong ultrashort magnetic pulses localized at the nanoscale. We show that a bimetallic nanoring illuminated by femtosecond laser pulses responds with transient thermoelectric currents of picosecond duration, which in turn induce Tesla-scale magnetic fields in the ring cavity. Our method provides a practical way of generating intense nanoscale magnetic fields with great potential for materials characterization, terahertz radiation generation and data storage applications.

---

[6] Author to whom any correspondence should be addressed.

Contents

1. Introduction

The study of ultrashort magnetic phenomena has been largely driven by their application to magnetic storage technologies, which are rapidly evolving toward the nanoscale and sub-picosecond regimes, giving rise to significant advances in the understanding of magnetization dynamics [1]. Currently, no easily accessible method is available to generate intense sub-picosecond magnetic pulses localized at the nanoscale. Short electron pulses can be tightly focused and are accompanied by magnetic fields of a few Teslas, but they require access to electron accelerators [2]. Transient magnetization has also been studied via the inverse Faraday effect, particularly in cases for which absorption of circularly polarized light leads to a prevailing spin species [3–5], and although this effect is also observed in non-absorbing materials [1], the spatial resolution is limited by the light focal spot. Here, we propose a radically new approach toward ultrafast magnetism with nanoscale resolution relying on optically driven generation of THz magnetic pulses.

In this work, we show that bimetallic nanorings can act as nanoscale sources of intense ultrashort magnetic pulses. We rely on the enhanced light absorption associated with the plasmons of metallic rings to generate transient thermoelectric currents that in turn produce sub-picosecond pulses with magnetic fields as high as a few tenths of a Tesla in the vicinity of the rings. The ability to generate strong magnetic fields localized on the nanoscale is of interest for elucidating spin and magnetization dynamics at sub-picosecond time and nanometer length scales [1], and it holds great potential for materials characterization, terahertz radiation generation and magnetic recording.

A scheme of our magnetic source is shown in figure 1. A 100 fs laser pulse heats a bimetallic ring consisting of three quadrants of gold and one quadrant of nickel. This choice of materials is a compromise between their thermoelectric response and their electrical resistance in order to optimize the resulting magnetic field. At the same time, gold is a good plasmonic material, while nickel has a reasonable level of absorption that is compatible with the existence

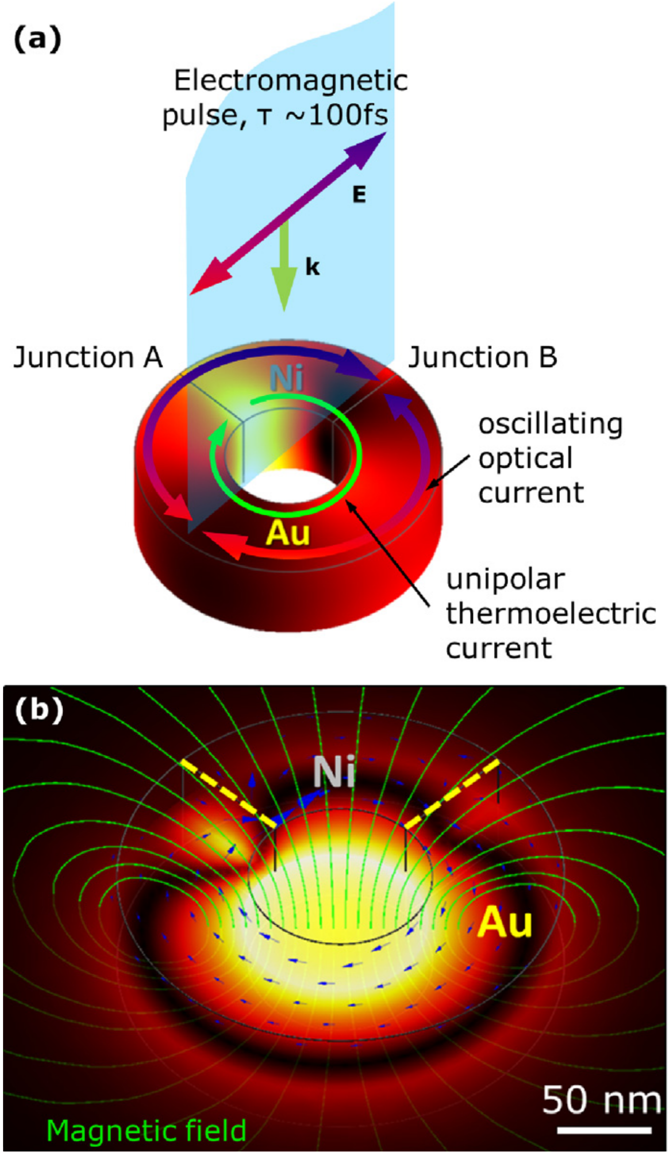

Figure 1. Schematic description of our nanoscale ultrashort strong magnetic-field source. (a) A femtosecond near-infrared laser pulse heats a bimetallic ring consisting of one quadrant of nickel and three quadrants of gold. At the plasmonic resonance of the ring, a dipole current oscillating at the incident light frequency is excited (blue/red arrows), leading to absorption and subsequent conduction-electron heating. A strong, non-oscillating thermoelectric current is then produced in this short-circuited thermocouple, driven by the conduction-electron temperature difference (∼ thousands of degrees) between the cold and hot Au/Ni junctions. (b) The thermoelectric ring current generates a strong magnetic field normal to the plane of the ring. The intensity of the magnetic-field component perpendicular to the ring plane is represented by the density plot, whereas magnetic-field lines are shown in green.

of a well-defined plasmon in the structure (see below). The ring is 100 nm thick, has an inner (outer) diameter of 70 nm (170 nm) and is embedded in glass. The incident pulse is polarized along one of the Au/Ni junctions (B in figure 1(a)) and is centered at a wavelength of 920 nm, which corresponds to the lowest-order dipole plasmon resonance of the ring. In a homogeneous gold ring, symmetry would lead to resonant absorption at two diametrically opposed regions. However, the asymmetry of the bimetallic ring polarization leads to stronger absorption near one of the Au/Ni junctions (A in figure 1(a)). This non-uniform absorption produces a steep gradient of the electron temperature along the ring, and consequently a net displacement of charge carriers occurs from hotter to colder regions, giving rise to a Seebeck electromotive force. In the Au/Ni thermocouple, charge carriers in gold and nickel are electrons and holes, respectively, so that the resulting thermoelectric current on either side of each metal junction flows along the same azimuthal direction [6]. Femtosecond pulses give rise to temperature differences of several thousand degrees in the conduction electron gas, as is well known in ultrafast studies of the optical response of heated metallic nanoparticles [7]. This results in a strong thermoelectric current before thermalization into the atomic lattice takes place within a few picoseconds. Finally, this transient circular current generates a magnetic field, mainly perpendicular to the plane of the ring (green lines in figure 1(b)). In a related context, thermoelectric detection of propagating plasmons has been recently reported [8], thus establishing a connection between plasmons and thermoelectric currents, which are exploited in this work to produce intense magnetic fields. Incidentally, the magnetic response of nickel to these fields could possibly act back on the thermoelectric current, although this effect lies outside the scope of this work. In contrast, as discussed below, self-inductance is expected to play a minor role.

We solve the underlying nonlinear heat-transfer/thermoelectric/electromagnetic problem within the two-temperature model [1, 6], assuming local thermal equilibrium, which allows us to define local lattice and electron temperatures, as well as an electron current density that we calculate from the thermal gradient and the temperature- and material-dependent Seebeck coefficient. The assumption of local thermal equilibrium breaks down at small distances [9], where a detailed account of ballistic diffusion must be taken into consideration [10], particularly near room temperature, for which hot electrons and holes near the Fermi level can travel long distances without scattering (e.g. $v_F\tau \sim 12$ nm is the inelastic mean free path in gold, as estimated from the Fermi velocity $\sim 1.4 \times 10^6$ m s^{-1} and the intrinsic optical Drude decay time $\tau \sim 9$ fs [11]; notice that this is a more relevant relaxation time for the hot electrons involved near the peak of optical excitation than the longer times estimated from dc measurements, which involve electrons that are extremely close to the Fermi level). This effect should be comparatively small for the high electron and hole energies associated with the elevated electron temperatures considered in this work. In addition, thermal equilibrium can take up to a few hundreds of femtoseconds to be established [12], so that ballistic transport and other transient effects can become relevant at sub-picosecond timescales [13]. For simplicity, we ignore these effects, which are beyond the scope of the present paper.

Our numerical simulations are obtained by using a commercial finite-element tool (COMSOL), and we supplement these results with a semi-analytical model that correctly predicts the magnitude of the generated field and its duration. The details of the relevant equations involved in the problem are given in appendix A, whereas the approximations made for the semi-analytical model are explained in appendix B (see equations (B.1) and (B.2)). The thermal and thermoelectric coefficients of nickel and gold, required to solve these equations, are plotted in appendices D and E.

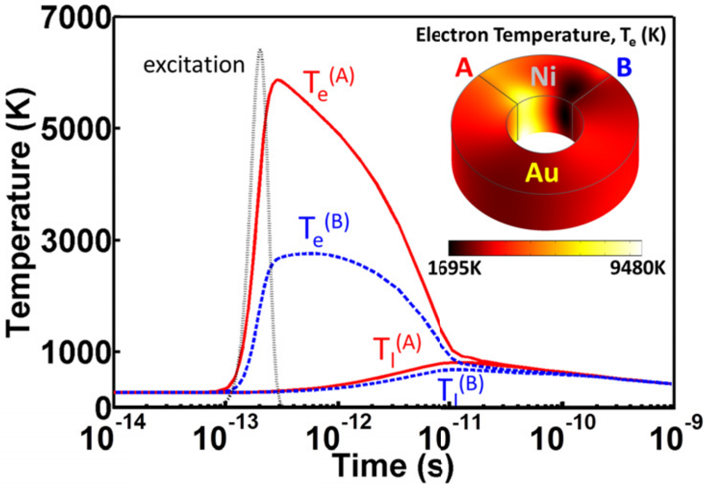

Figure 2. Temporal temperature profiles upon irradiation by a light pulse. Electron (T_e) and lattice (T_l) temperatures at the hot (solid red, A) and cold (dashed blue, B) junctions of the ring. The pulse fluence is 11.3 J m^{-2} and evolves as shown by the dotted curve. A snapshot of the electron temperature on the ring surface is shown in the inset at the time corresponding to the maximum of T_e in the hot junction A.

2. Results and discussion

The time evolution of the conduction-electron (T_e) and lattice (T_l) temperatures at the two Au/Ni junctions is shown in figure 2 for an incident pulse fluence of 11.3 J m^{-2}, which transfers ~1.4 pJ to the ring (absorption cross-section ~0.12 μm^2, see appendix C). Following an initial excitation with the ultrafast optical pulse, the electron-gas temperature rapidly rises at both junctions, reaching peak values shortly after the maximum of the incident pulse. The nickel section of the ring produces a considerable temperature difference between the two junctions: electrons at the hot junction (A) reach a peak temperature of ~6000 K, which is approximately twice the temperature of the cold junction electrons (B). The peak temperature at B occurs nearly 1 ps after the maximum of A as a result of hot-electron diffusion. Over this short time interval, the absorbed energy remains almost entirely in the electron gas, while thermalization of the gold and nickel lattices, initially at 300 K, takes place over a timescale of several picoseconds [14]. The lattice and electron temperatures become nearly identical ~10 ps after irradiation, when both junctions are at ~600 K, well below the melting temperature of the ring materials. Finally, the ring cools back to room temperature after a few nanoseconds due to diffusion through the surrounding glass.

The decay from maximum heating reveals three different timescales: a fast decay (~1 ps) produced by thermal diffusion within the electron gases of the two metals; an intermediate decay (~10 ps) that can be ascribed to thermalization of the electrons into the lattice via electron–phonon scattering; and a slow decay (~nanoseconds) arising from thermalization into the surrounding glass. This picture is consistent with the temperature dependence of the involved materials parameters (see appendix).

The temperature gradient between two junctions of metals with different Seebeck coefficients produces an electromotive force that drives a thermoelectric current along the ring

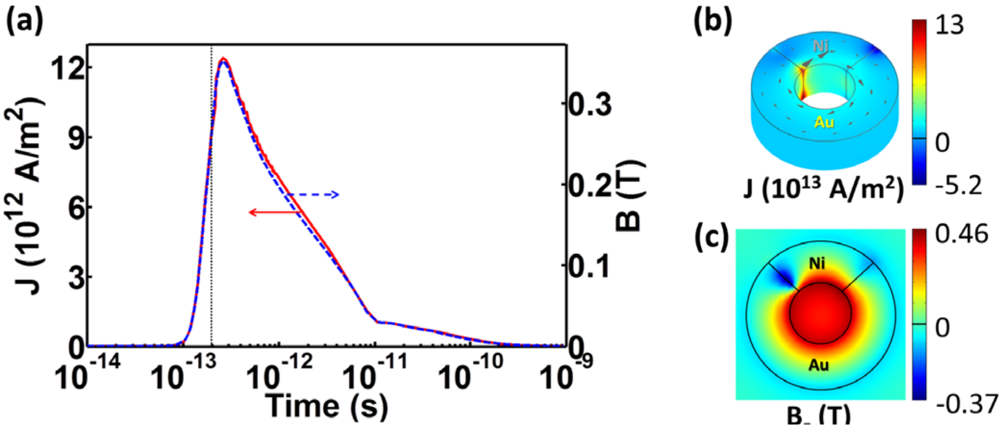

Figure 3. Temporal thermoelectric current and magnetic field profiles. (a) We show the time evolution of the azimuthal component of the current through junction A (dashed curve, left scale) and the magnetic induction averaged over the ring hole (solid curve, right scale). The dotted vertical line indicates the maximum of the light pulse intensity. (b), (c) Snapshots of the instantaneous current on the ring surface (b) and the axial component of the magnetic induction (c), both at the time of the maximum of the curves in (a). The irradiation conditions are the same as in figure 2.

circumference. For uniformly heated junctions, this effect is quantified through a potential between them $S\Delta T$, proportional to the temperature difference ΔT. The Seebeck coefficient S depends on the nature of the material between the two junctions, as well as on temperature (see appendix E). Owing to the high electron temperatures involved, the thermoelectric current density in the confined ring geometry reaches values as high as $\sim 10^{13}\,\mathrm{A\,m^{-2}}$. Figure 3(a) (left scale) illustrates the temporal evolution of the current density through junction A, which follows quite closely the temperature difference, with a maximum occurring $\sim$100 fs after the peak of the excitation pulse. The current distribution on the ring surface (figure 3(b)) reveals a dominant azimuthal component, except near the hot junction, where parasitic short-range loops are produced.

These strong currents give rise to a large magnetic induction (>0.35 T peak value) of a similar temporal profile (figure 3, right scale). The induction is localized inside the ring cavity (figure 3(c)), where it is rather uniform (figure 4, inset), with the exception of a depletion caused by the noted loop currents in the hot Au/Ni junction. This uniformity is similar to the field produced by magnetic resonances in split-ring resonators driven by externally applied radiation [15]. The magnetic pulse has a duration $\Delta t_{\mathrm{mag}} \sim 1.8$ ps full-width at half-maximum (FWHM), mainly controlled by electron diffusion and thermalization into the lattice (see appendix B).

The peak magnetic induction grows monotonically with light-pulse fluence (figure 4), exhibiting slightly sub-linear behavior as a result of the increase in electron heat capacity with temperature [6], although the net effect involves a complex interplay between the temperature dependence of the materials thermal and electrical parameters (see appendices D and E).

We have formulated a simple model that yields semi-analytical expressions for the peak magnetic induction (equation (B.1)) and the magnetic pulse duration (equation (B.2)), as

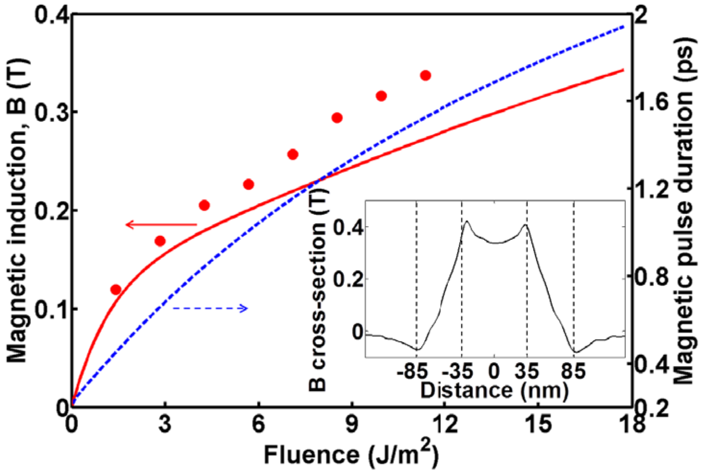

Figure 4. Magnetic-field strength and magnetic-pulse duration as a function of light-pulse fluence. We represent the calculated maximum of the magnetic induction (left vertical scale) as a function of incident pulse fluence from full numerical simulations (symbols) and from the semi-analytical model described in appendix B (solid curve, equation (B.1)). The FWHM duration of the magnetic pulse (right vertical scale) is estimated from the analytical model (dashed curve, equation (B.2)). The inset shows a characteristic profile of the magnetic induction across the ring.

discussed in appendix B. The model is based upon the neglect of thermal diffusion in the lattice and it assumes that the optical pulse acts as a sudden impulse. This produces results in excellent agreement with full numerical simulations, as shown in figure 4, thus providing a simple tool that can assist in the design of rings optimized in size and composition to yield the desired levels of magnetic pulse intensity and duration. In particular, the model predicts a magnetic field duration that increases with optical pulse fluence, which essentially reflects the decrease in electron–phonon coupling and the increase in the heat capacity associated with the ever larger electron temperature that is reached with higher pumping intensities (see appendix F).

3. Conclusions and outlook

Our results indicate that we can take advantage of the strong thermoelectric currents at the nanoscale in order to achieve very intense, transient, THz electromagnetic fields driven by pumping with vis–NIR light. This can be the basis of a new source of optically pumped THz radiation, whereby illuminated rings act as localized magnetic dipoles. Magnetic polarization has been previously used to generate THz radiation [16, 17], but the magnetic dipoles have a fundamentally different origin in our proposed scheme relying on thermoelectric currents. In a different, important range of applications, illuminated bimetallic rings provide an interesting opportunity for nanoscale magnetic recording triggered by the intense magnetic field (strongly confined in the <100 nm ring cavity) in combination with suitable magnetic grain sizes that can react to the short duration of the magnetic pulse [2]. As a practical consideration, the main limitation on the values of the achievable magnetic field comes from the breakdown current in the rings ($\sim 10^{12}$–10^{13} A m^{-2} for gold [18, 19]), as well as from possible melting of the metals [20]. However, the short duration of the optical irradiation, the moderate lattice temperatures involved and the embedding of the ring in a rigid glass matrix (e.g. in a good thermal conductor such as silica or diamond) should push the thresholds for melting and electrical breakdown well beyond the currents and temperatures considered here. In fact, the breakdown current increases dramatically with decreasing wire width, to an estimated dc value of $\sim 6 \times 10^{12}\,\mathrm{A\,m^{-2}}$ [21] for the width of the ring walls under consideration. It should also be mentioned that electromigration is the main breakdown mechanism [21], and thus it requires periods of time that are orders of magnitude larger than the picosecond timescale considered here. Additional ohmic losses can occur at the metal interfaces; using values of the contact resistance reported in recent literature [22, 23], we estimate the reduction in the thermoelectric current to be a factor of 2 at most.

It should be pointed out that, although we focus on thermoelectric current generation, other mechanisms can contribute with additional sub-picosecond currents, such as for instance the fast changes in the magnetization of nickel under the influence of the generated quasi-dc magnetic field. In addition, spin transport triggered by the laser excitation due to spin–orbit coupling can produce transverse currents [24], which we estimate to be weaker than the thermoelectric current.

In conclusion, we have shown that a bimetallic nanoring illuminated by ultrafast laser pulses supports transient thermoelectric currents leading to magnetic pulses of sub-picosecond duration reaching a fraction of a Tesla and localized in the $< 100\,\mathrm{nm}$ ring cavity. Our results can facilitate the study of ultrafast, nanoscale magnetic phenomena, and they hold great potential for applications in materials characterization, the generation of terahertz radiation and magnetic recording.

Acknowledgments

This work has been supported in part by the Engineering and Physical Sciences Research Council (UK), the Leverhulme Trust, the Royal Society and the Spanish MEC (MAT2010-14885 and Consolider NanoLight.es).

Appendix A. Formulation of the model

Our simulations of optically induced generation of magnetic fields mediated by thermoelectric currents in bimetallic rings involve solving a set of coupled equations for (i) the electromagnetic field intensity of the incident light, (ii) the heat diffusion problem, (iii) the resulting thermoelectric current and (iv) the magnetic field itself. In this work, we provide two levels of theory based upon (i) full numerical simulations and (ii) semi-analytical modeling. We use a commercial finite-element method (COMSOL) for the former, whereas a derivation of the latter is summarized below. But first, we discuss the relevant equations and approximations required to deal with each of the four noted sub-problems.

A.1. Light-pulse absorption by the ring

Light absorption is calculated by solving Maxwell's equations for a Gaussian pulse of $\sim 2\Delta t_{\mathrm{pulse}} = 100\,\mathrm{fs}$ duration centered at a wavelength of 920 nm and incident on the ring along its axis with linear polarization as shown in figure 1. Because the pulse duration is much longer than the light period (3.1 fs), the absorbed power density (i.e. the position- and time-dependent power absorbed per unit volume inside the ring) is approximated as $p(\mathbf{r},t) = p(\mathbf{r}) f(t)$, assuming that it follows the pulse temporal profile $f(t) = \exp[-t^2/(\Delta t_{\mathrm{pulse}})^2]$, multiplied by the peak absorption density $p(\mathbf{r})$, which we calculate for a plane wave with the same intensity as the pulse maximum. The dielectric functions of gold $(-33.56 - 1.93\mathrm{i})$, nickel $(-15.47 - 26.03\mathrm{i})$ and glass (2.1) are taken from tabulated optical data [25].

A.2. Thermal diffusion and temperature distribution

The absorbed power density $p(\mathbf{r},t)$ acts as the source of heat for the thermal diffusion problem. We adopt a two-temperature model [6], in which the conduction-electron and atomic-lattice subsystems have their own temperatures $T_{\mathrm{e}}(\mathbf{r},t)$ and $T_{\mathrm{l}}(\mathbf{r},t)$, respectively, each of them evolving over very different timescales. We assume that the heating produced through $p(\mathbf{r},t)$ is entirely transferred from the light to the conduction electrons, which reach local thermal equilibrium in a short time compared with the characteristic times for thermal diffusion and lattice thermalization (see below). The thermal diffusion equation is then simultaneously solved for the electronic and lattice sub-systems, which are coupled through a term accounting for heat transfer from the former to the latter. We assume this term to be proportional to the local temperature difference $T_{\mathrm{e}} - T_{\mathrm{l}}$, via an electron–phonon coupling coefficient G. This leads to the two coupled diffusion equations [6]

$$c_{\mathrm{e}} \frac{\mathrm{d}T_{\mathrm{e}}}{\mathrm{d}t} = \nabla(\kappa_{\mathrm{e}} \nabla T_{\mathrm{e}}) - G\,(T_{\mathrm{e}} - T_{\mathrm{l}}) + p, \tag{A.1}$$

$$c_{\mathrm{l}} \frac{\mathrm{d}T_{\mathrm{l}}}{\mathrm{d}t} = \nabla(\kappa_{\mathrm{l}} \nabla T_{\mathrm{l}}) + G\,(T_{\mathrm{e}} - T_{\mathrm{l}}), \tag{A.2}$$

where c_{e} and c_{l} are the electron and lattice heat capacities, and κ_{e} and κ_{l} are the respective thermal conductivities. We use values of the temperature-dependent coefficients C, κ and G for Ni and Au compiled from the literature [6, 26–30], as discussed in appendices D and E. For simplicity, we ignore the effect of heterojunction thermal barriers, which should contribute to create higher temperature gradients and stronger magnetic fields.

A.3. Thermoelectric current

From the solution of equations (A.1) and (A.2), we derive a thermoelectric electromotive force $S \nabla T_{\mathrm{e}}$, where S is the Seebeck coefficient. This allows us to write the thermoelectric current as

$$\mathbf{j} = \sigma\,(S \nabla T_{\mathrm{e}} - \nabla V)\,, \tag{A.3}$$

where σ is the temperature-dependent electric conductivity and V represents the potential displayed in response to the thermoelectric source. We use values for the temperature-dependent coefficients S and σ for Ni and Au calculated from [6, 31], as explained in appendix E. Since T_{e} varies smoothly over hundreds of femtoseconds, involving characteristic frequencies below the mid-infrared, we can safely assume that the metals behave as good conductors, so that the thermoelectric current is quasi-stationary and the continuity equation reduces to the vanishing of $\nabla \cdot \mathbf{j}$ (this is equivalent to neglecting the self-inductance of the thermoelectric current). Inserting equation (A.3) into this expression, we find

$$\nabla \cdot \sigma \nabla V = \nabla \cdot \sigma S \nabla T_{\mathrm{e}}, \tag{A.4}$$

which is formally equivalent to Poisson's equation with a local response function σ and a source term $-\nabla \cdot \sigma S \nabla T_e$. Incidentally, by setting $\sigma = 0$ outside the ring, equation (A.4) guarantees the vanishing of the normal current at the ring boundaries. We obtain V by solving equation (A.4), and this is in turn inserted into equation (A.3) to yield $\mathbf{j}$.

A.4. Magnetic induction

Finally, we use the electric current $\mathbf{j}$ (equation (A.3)) to find the resulting magnetic induction from [32]

$$\mathbf{B}(\mathbf{r}, t) = \frac{\mu_0}{4\pi} \int \mathrm{d}^3\mathbf{r}' \, \frac{\mathbf{j} \times (\mathbf{r} - \mathbf{r}')}{|\mathbf{r} - \mathbf{r}'|^3}, \tag{A.5}$$

where the integral is extended over the volume of the ring.

Appendix B. Semi-analytical model

A simple model that predicts the order of magnitude of the generated magnetic field, the current circulating around the ring and the duration of the magnetic pulse can be formulated under the following approximations.

B.1. Sudden pulse excitation

Upon inspection of equation (A.1), we expect to have characteristic diffusion and thermalization times given by $\Delta t_{\mathrm{dif}} = R^2 c_e/\kappa_e$ and $\Delta t_{\mathrm{th}} = c_e/G$, respectively, where R is the average ring radius. For the high temperatures ($T_e > 2000\,\mathrm{K}$) at which a large magnetic field is generated, we have $\Delta t_{\mathrm{dif}} > 0.5\,\mathrm{ps}$ and $\Delta t_{\mathrm{th}} > 2\,\mathrm{ps}$, in front of which we neglect $\Delta t_{\mathrm{pulse}} = 50\,\mathrm{fs}$, and thus we consider the pulse to deliver an instantaneous impulse quantified by an absorbed energy density $q = \sqrt{\pi}\,\Delta t_{\mathrm{pulse}}\, p(\mathbf{r})$. This determines the maximum local electron temperature T_e right after pulse irradiation by imposing $q = \int_{T_0}^{T_e} c_e(T)\,\mathrm{d}T$, where T_0 is the initial room temperature before irradiation.

B.2. Neglect of the lattice

Upon examination of the physical parameters entering equations (A.1) and (A.2) (see appendices D and E), we observe that $\kappa_l \ll \kappa_e$ and $c_l \gg c_e$, that is, the lattice takes much more heat to increase its temperature than the electron gas and it conducts heat more poorly. This explains why $T_l \ll T_e$ during the bulk of the magnetic pulse duration, so we can safely ignore the lattice and reduce equation (A.1) to $c_e\,\mathrm{d}T_e/\mathrm{d}t = \nabla(\kappa_e \nabla T_e) - G\,T_e$, with the initial condition for $T_e(t = 0)$ derived above.

B.3. Average over ring cross-section

We can further assume that the temperature distribution can be well represented if we replace it by its azimuthal-angle-dependent average over the radial and vertical directions (i.e. the average over the ring cross-section). We then focus on the azimuthal component of the current j, which we can take as uniform along the ring circumference as a consequence of the vanishing of $\nabla \cdot \mathbf{j}$. Noticing that the potential V must reach the same value when ∇V is integrated along a whole ring circumference, we find from equation (A.3) that $j\int \mathrm{d}\varphi/\sigma = (1/R)\int S(\partial T_\mathrm{e}/\partial\varphi)\mathrm{d}\varphi$, where we have approximated the azimuthal component of ∇ as $(1/R)\partial/\partial\varphi$. Finally, we can carry out the integral on the right-hand side of this equation from junction A to B through Au and from B to A through Ni (see figure 2(a)). This produces the expression

$$B = \frac{\mu_0}{4\pi}\,\beta\,\frac{\int_{T_\mathrm{B}}^{T_\mathrm{A}} \mathrm{d}T\,[S_\mathrm{Au}(T) - S_\mathrm{Ni}(T)]}{\int \mathrm{d}\varphi/\sigma} \tag{B.1}$$

for the z component of the magnetic induction at the ring center, where $\beta = (1/R)\int \mathrm{d}\mathbf{r}\,\hat{\mathbf{z}}\cdot(\hat{\varphi}\times\mathbf{r})/r^3$ is a dimensionless geometrical factor ($\beta \approx V/R^3$, where V is the ring volume).

Following the discussion in point (i), we estimate the pulse duration from the diffusion and thermalization times as

$$\Delta t_\mathrm{mag} = \left\langle \frac{1}{1/\Delta t_\mathrm{dif} + 1/\Delta t_\mathrm{th}} \right\rangle, \tag{B.2}$$

where the brackets stand for the average along the ring circumference, which needs to be taken due to the strong dependence of Δt_dif and Δt_th on the local electron temperature. We show in figure 4 the pulse duration evaluated from equation (B.2) right after irradiation.

Appendix C. Plasmon resonance in the gold–nickel ring

The inhomogeneous ultrafast heating of the ring relies on one of its plasmon resonances. We show in figure C.1 the absorption spectrum of the ring under the same conditions of illumination as considered in figure 1. The spectrum shows a well-defined plasmon that is peaked at 920 nm. This corresponds to the wavelength of the resonant laser. The figure also illustrates the near field associated with this plasmon, which exhibits a clear dipolar pattern, although it is asymmetric due to the inhomogeneous composition of the ring. In particular, the two Au/Ni junctions are exposed to different levels of near-field intensity, which is maximum near one of them outside the ring and near the other one inside the metal, leading to a net difference in heating temperature.

Appendix D. Thermal parameters

The parameters describing heat diffusion in both the electronic and lattice sub-systems of Ni and Au are plotted in figure D.1, along with the coefficient for electron–lattice thermalization. These parameters depend on the electron temperature. In addition, the electron thermal conductance depends on the lattice temperature.

The temperature-dependent electron heat capacities are taken from [6] (figure D.1(a)), whereas the lattice heat capacity for Au is taken from [26] (figure D.1(b)). However, there is little information available on the temperature dependence of the lattice heat capacity for Ni, and since the lattice temperature is only mildly affecting our final results and the range of lattice temperatures is limited to ~300–600 K, we have approximated it by a constant value measured at room temperature [27].

We approximate the electron thermal conductivity (figure D.1(c)) from the Drude model as [28]

$$\kappa_\mathrm{e} = \frac{1}{3}c_\mathrm{e}v_\mathrm{F}^2\tau, \tag{D.1}$$

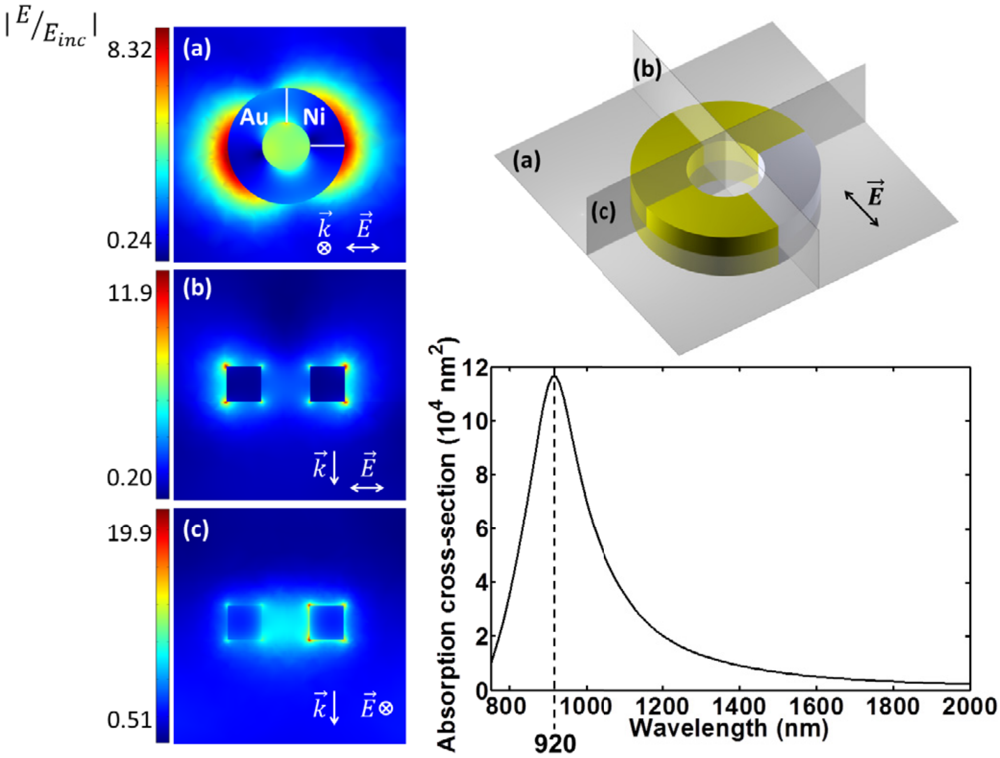

Figure C.1. Plasmon resonance in the Ni–Au ring. Electromagnetic simulation of the response of the same glass-embedded ($\epsilon = 2.1$) heterogeneous ring as considered in figure 1. The absorption cross-section spectrum shows a well-defined plasmon resonance peaking at 920 nm. The near-field amplitude maps on the left hand side of the figure reveal the dipolar character and asymmetric intensity of the plasmon. The directions of the incident electric field and light propagation are indicated by labels. The planes on which the near-field intensity is represented are schematically illustrated in the upper-right sketch.

where v_F is the Fermi velocity ($1.40 \times 10^6\,\mathrm{m\,s^{-1}}$ in Au [28] and $0.28 \times 10^6\,\mathrm{m\,s^{-1}}$ in Ni [33]) and τ is the electron scattering rate. The latter is approximated as [29]

$$\tau = \frac{1}{A_e {T_e}^2 + B_l T_l}, \qquad \text{(D.2)}$$

where $A_e = 1.2 \times 10^7$ and $B_l = 1.23 \times 10^{11}$ for Au [29] and $A_e = 1.4 \times 10^6$ and $B_l = 1.624 \times 10^{13}$ for Ni [30], all in SI units with the temperatures in Kelvin. The lattice thermal conductivity (figure D.1(d)) is taken from [26] for Au and approximated as a constant for Ni [27] for the reasons discussed above. Finally, the electron–lattice coupling coefficient G (figure D.1(e)) is taken from [6].

From the form of equations (A.1) and (A.2), we can extract two characteristic times $\Delta t_{\mathrm{dif}} = R^2 c_e/\kappa_e$ and $\Delta t_{\mathrm{th}} = c_e/G$ associated with heat diffusion and thermalization, respectively. Here, $R = 60$ nm is the average radius of the ring. We plot these times in figure D.2 as a function of electron temperature using the parameters of figure D.1. Both these types of processes are thus

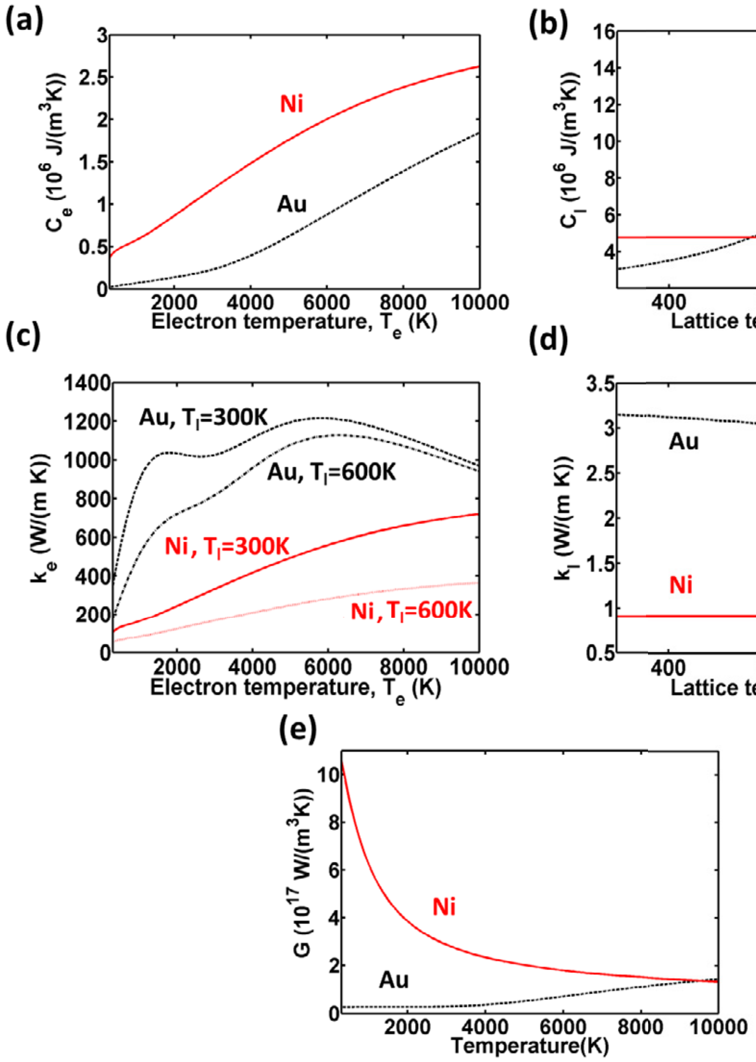

Figure D.1. Thermal parameters used in the description of heat diffusion for Ni and Au. (a), (b) Electronic [6] and lattice [26, 27] heat capacities, c_e and c_l, respectively. (c), (d) Electronic [28–30] and lattice [26, 27] thermal conductivities, κ_e and κ_l, respectively. (e) Electron–lattice coupling coefficient [6], G.

expected to have a similar influence on the temporal decay of the high-temperature gradient following light-pulse irradiation.

Appendix E. Electrical and thermoelectrical parameters

The Seebeck coefficient S and the electrical conductivity σ are calculated from the electronic density of states (taken from [6] for Au and Ni), conveniently weighted by the Fermi–Dirac distribution for each temperature T_e, following the prescription described in [31]. Both S and σ exhibit a pronounced electron-temperature dependence, as shown in figure E.1.

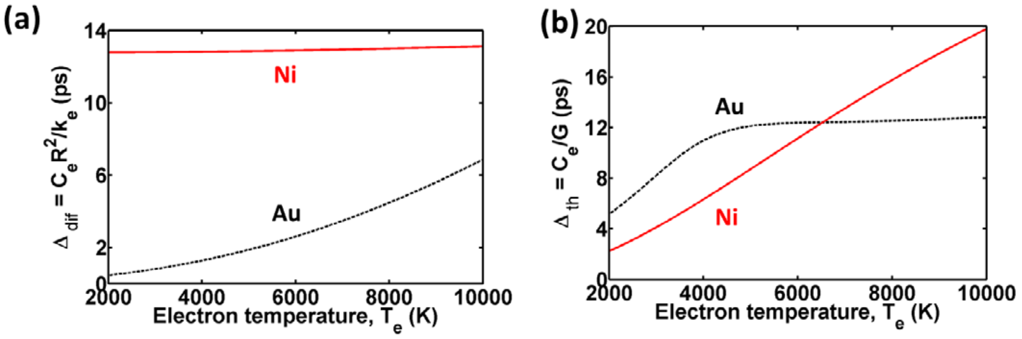

Figure D.2. Diffusion and thermalization. Estimates of the local (a) diffusion and (b) thermalization times based on the coefficients of figure C.1 and their involvement in equations (A.1) and (A.2).

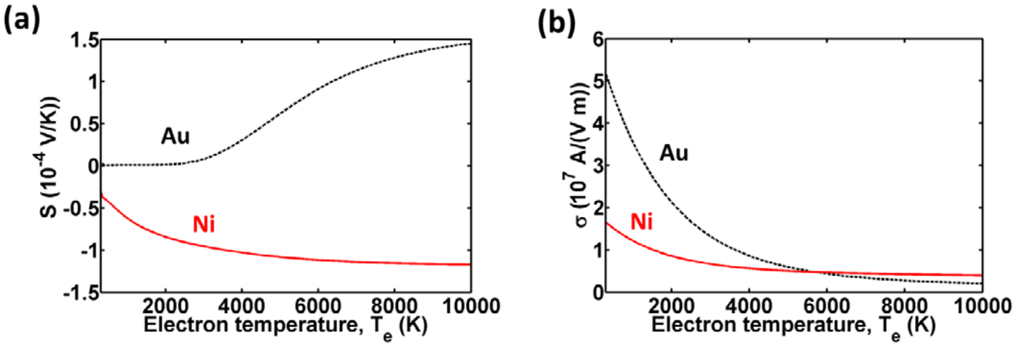

Figure E.1. Electrical and thermoelectrical properties. Temperature dependence of (a) the Seebeck coefficient [31] and (b) the electrical conductivity [6, 31].

Appendix F. Optical heating

We calculate the absorption power density $p(\mathbf{r})$ in the ring upon illumination by a plane wave of intensity 10^{14} W m^{-2}, linearly polarized with the electric field along the x-axis (i.e. azimuthal angle 0, coinciding with one of the Au/Ni junctions). The absorption density is simply scaled with the temporal profile of the light pulse, as explained in appendix A. The entire $\mathbf{r}$ dependence of $p(\mathbf{r})$ is used in our full numerical simulations, whereas we average this quantity over the cross-section of the ring as an input for the semi-analytical model. The averaged absorption density exhibits pronounced maxima at the Au/Ni junctions (figure F.1) and clearly reveals the hot junction at an azimuthal angle of $\pi/2$ (i.e. where the current at the optical frequency is maximum upon excitation of a dipole plasmon along the x-axis). The overall absorption is quantified by an effective cross-section of $\sim 0.12\,\mu$m^2.

The distribution of the electron temperature along the ring circumference is shown in figure F.2 as a function of pulse fluence, as obtained from the semi-analytical model, averaged over the ring-cross-section. Nonlinear dependence on fluence is clearly observed.

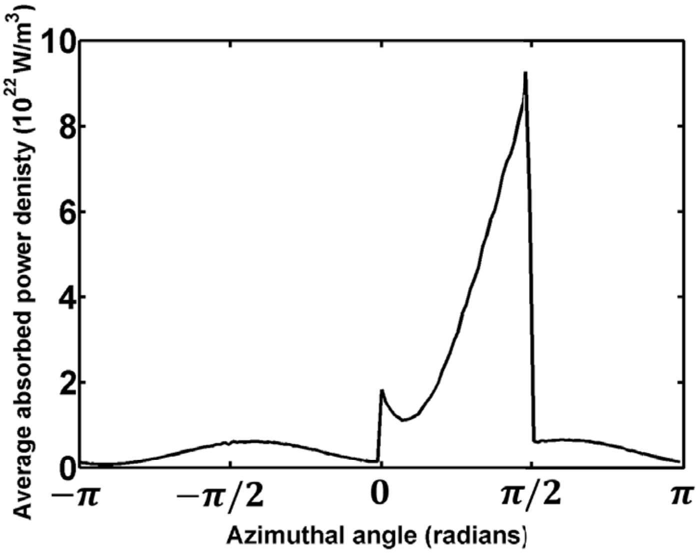

Figure F.1. Absorbed power density. We plot the average of this quantity over the ring cross-section as a function of the azimuthal angle along the ring considered in figure 1 for illumination with a plane wave of intensity 10^{14} W m^{-2} at the resonance wavelength of 920 nm. The external field is linearly polarized along the 0 azimuthal-angle direction, which coincides with one of the Ni/Au junctions. The other junction is at angle $\pi/2$, as shown in figure 1.

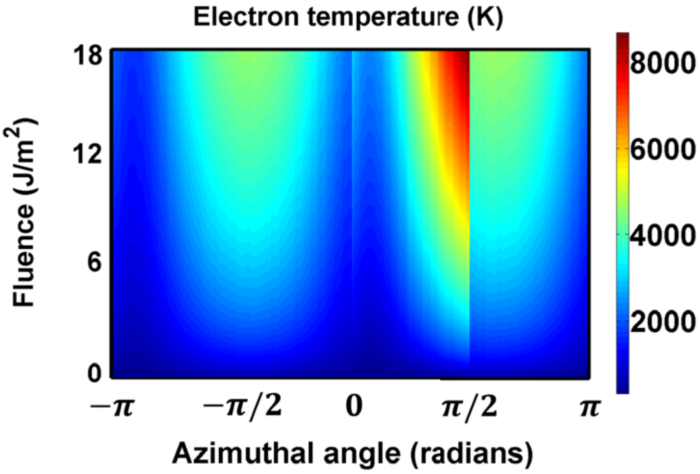

Figure F.2. Distribution of the electron temperature along the ring circumference right after light-pulse irradiation as a function of pulse fluence, according to the semi-analytical model described in appendix B.

Appendix G. Thermoelectrical current

We show in figure G.1 the thermoelectric current obtained from the semi-analytical model (solid curve), as compared with full numerical simulations (symbols). In the semi-analytical model, the generated magnetic field (see figure 4) follows exactly the same profile as the current, whereas the full simulation shows minor differences between the two profiles due to the finite spatial extension of the current over the cross-section of the ring.

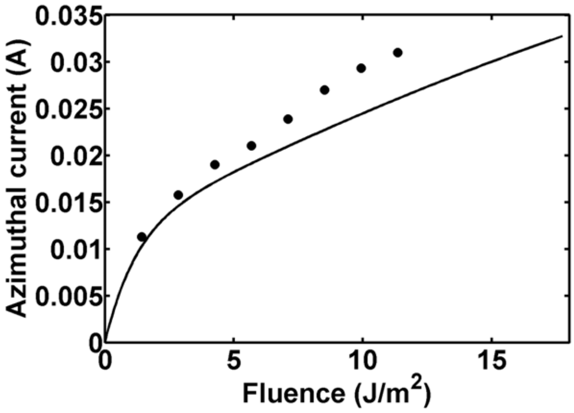

Figure G.1. Electrical current circulating around the ring right after light-pulse irradiation as a function of pulse fluence, obtained from the semi-analytical model (curve) and from full numerical simulations (symbols).

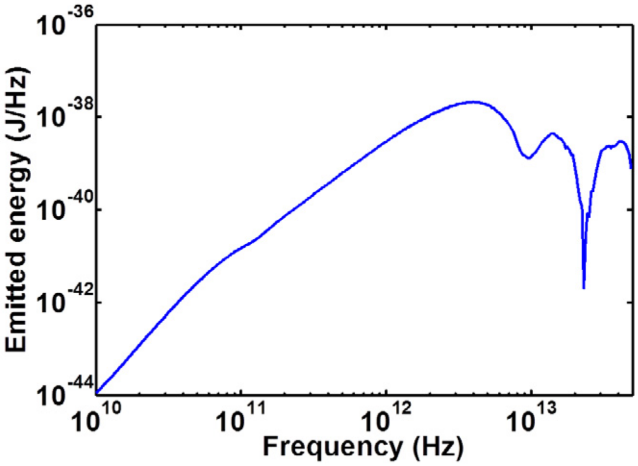

Figure H.1. Radiation emission spectrum produced by the thermoelectric current. We show the energy radiated by the thermoelectric current per unit of emission frequency range. The light pulse fluence is 11.3 J m^{-2}. The total absorbed energy is then 1.3 pJ per ring per pulse, whereas the emitted energy (integral of the plotted curve) is only 10^{-12} times that value.

The current density (e.g., $\sim 5 \times 10^{12}$ A m^{-2} for a fluence of 2 J m^{-2}) is above the threshold for materials damage ($\sim 10^{12}$ A m^{-2} from the measurements in nanowires under dc conditions [18]). However our ring is only exposed to it for a short interval, well below the characteristic timescale for structural changes in the metals. Embedding of the ring in a hard, transparent material can be a good strategy for increasing the damage threshold.

Appendix H. Radiated energy

The transient thermoelectric current produces radiation that is expected to be roughly peaked at a frequency corresponding to the inverse of the temporal width of the heating peak. The calculated radiation energy per unit of emission frequency, which is represented in figure H.1,

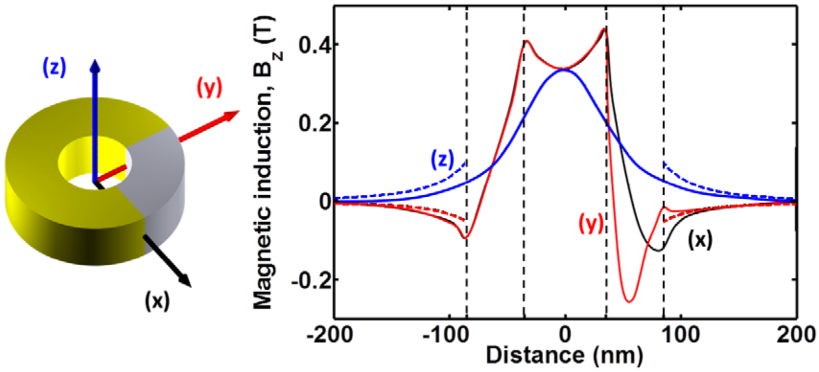

Figure I.1. Spatial distribution of the generated magnetic field near the ring. We show the z component of the magnetic field produced by the thermoelectric current at the peak intensity along the directions indicated in the right sketch. Solid curves: full numerical calculation. Broken curves: magnetic field generated by the calculated dipole placed at the center of the ring.

fully corroborates this intuition. This constitutes an innovative way of generating THz radiation, although the efficiency of the emission is small compared to the energy dissipated via relaxation to the lattice.

Appendix I. Spatial distribution of the generated magnetic field

The spatial distribution of the peak magnetic field is shown in figure I.1, where it is observed to decay with distance roughly as a static dipole. The solid curves (full numerical calculation) agree well with the result obtained from a dipole sitting at the center of the ring and whose magnitude is obtained from the integrated thermoelectric current, although some deviations toward large distances are observed because of the presence of neighboring rings in the numerical simulation (i.e. this is performed for a periodic array), which are not present in the analytical dipole field.

References

[1] Kirilyuk A, Kimel A V and Rasing T 2010 Ultrafast optical manipulation of magnetic order *Rev. Mod. Phys.* **82** 2731–84

[2] Tudosa I, Stamm C, Kashuba A B, King F, Siegmann H C, Stohr J, Ju G, Lu B and Weller D 2004 The ultimate speed of magnetic switching in granular recording media *Nature* **428** 831–3

[3] Fadley C S and Bergström S Å L 1971 Magnetization induced by optical pumping in antiferromagnetic MnF_2 *Phys. Rev. Lett.* **26** 652–5

[4] Kimel A V, Kirilyuk A, Usachev P A, Pisarev R V, Balbashov A M and Rasing T 2005 Ultrafast non-thermal control of magnetization by instantaneous photomagnetic pulses *Nature* **435** 655–7

[5] Hansteen F, Kimel A, Kirilyuk A and Rasing T 2006 Nonthermal ultrafast optical control of the magnetization in garnet films *Phys. Rev.* B **73** 014421

[6] Lin Z, Zhigilei L V and Celli V 2008 Electron–phonon coupling and electron heat capacity of metals under conditions of strong electron–phonon nonequilibrium *Phys. Rev.* B **77** 075133

[7] Perner M, Bost P, Lemmer U, von Plessen G, Feldmann J, Becker U, Mennig M, Schmitt M and Schmidt H 1997 Optically induced damping of the surface plasmon resonance in gold colloids *Phys. Rev. Lett.* **78** 2192–5

[8] Weeber J-C, Hassan K, Bouhelier A, Colas des Francs G, Arocas J, Markey L and Dereux A 2011 Thermoelectric detection of waveguided surface plasmon propagation *Appl. Phys. Lett.* **99** 031113

[9] Brorson S D, Fujimoto J G and Ippen E P 1987 Femtosecond electronic heat-transport dynamics in thin gold films *Phys. Rev. Lett.* **59** 1962–5

[10] Kaltenborn S, Zhu Y-H and Schneider H C 2012 Wave-diffusion theory of spin transport in metals after ultrashort-pulse excitation *Phys. Rev.* B **85** 235101

[11] Johnson P B and Christy R W 1972 Optical constants of the noble metals *Phys. Rev.* B **6** 4370–9

[12] Fann W S, Storz R, Tom H W K and Bokor J 1992 Electron thermalization in gold *Phys. Rev.* B **46** 13592–5

[13] Battiato M, Carva K and Oppeneer P M 2012 Theory of laser-induced ultrafast superdiffusive spin transport in layered heterostructures *Phys. Rev.* B **86** 024404

[14] Koopmans B, Malinowski G, Dalla Longa F, Steiauf D, Fähnle M, Roth T, Cinchetti M and Aeschlimann M 2010 Explaining the paradoxical diversity of ultrafast laser-induced demagnetization *Nature Mater.* **9** 259–65

[15] Della Valle G and Bozhevolnyi S I 2012 Efficient suppression of radiation damping in individual plasmonic resonators: towards high-*q* nano-volume sensing *Ann. Phys.* **524** 253–72

[16] Beaurepaire E, Turner G M, Harrel S M, Beard M C, Bigot J-Y and Schmuttenmaer C A 2004 Coherent terahertz emission from ferromagnetic films excited by femtosecond laser pulses *Appl. Phys. Lett.* **84** 3465–7

[17] Nishitani J, Kozuki K, Nagashima T and Hangyo M 2010 Terahertz radiation from coherent antiferromagnetic magnons excited by femtosecond laser pulses *Appl. Phys. Lett.* **96** 221906

[18] Karim S, Maaz K, Ali G and Ensinger W 2009 Diameter dependent failure current density of gold nanowires *J. Phys. D: Appl. Phys.* **42** 185403

[19] Yao H, Duan J, Mo D, Günel H Y, Chen Y, Liu J and Schäpers T 2011 Optical and electrical properties of gold nanowires synthesized by electrochemical deposition *J. Appl. Phys.* **110** 094301

[20] Inasawa S, Sugiyama M and Yamaguchi Y 2005 Laser-induced shape transformation of gold nanoparticles below the melting point: the effect of surface melting *J. Phys. Chem.* B **109** 3104–11

[21] Durkan C, Schneider M A and Welland M E 1999 Analysis of failure mechanisms in electrically stressed Au nanowires *J. Appl. Phys.* **86** 1280–6

[22] Ozturk B, Flanders B N, Grischkowsky D R and Mishima T D 2007 Single-step growth and low resistance interconnecting of gold nanowires *Nanotechnology* **18** 175707

[23] Stavitski N, Klootwijk J H, van Zeijl H W, Kovalgin A Y and Wolters R A M 2009 Cross-bridge Kelvin resistor structures for reliable measurement of low contact resistances and contact interface characterization *IEEE Trans. Semicon. Manu.* **22** 146–52

[24] Kampfrath T *et al* 2013 Terahertz spin current pulses controlled by magnetic heterostructures *Nature Nanotechol.* **8** 256–60

[25] Palik E D 1985 *Handbook of Optical Constants of Solids* (San Diego, CA: Academic)

[26] Huang J, Zhang Y and Chen J K 2009 Ultrafast solid–liquid–vapor phase change of a gold film induced by pico- to femtosecond lasers *Appl. Phys.* A **95** 643–53

[27] Lide D R 2005 *Handbook of Chemistry and Physics* (Boca Raton, FL: CRC)

[28] Ashcroft N W and Mermin N D 1976 *Solid State Physics* (New York: Harcourt College Publishers)

[29] Chen J K, Latham W P and Beraun J E 2005 The role of electron–phonon coupling in ultrafast laser heating *J. Laser Appl.* **17** 63–8

[30] Ivanov D S and Zhigilei L V 2003 Combined atomistic-continuum modeling of short-pulse laser melting and disintegration of metal films *Phys. Rev.* B **68** 064114

[31] Hopkins P E, Bauer M L, Duda J C, Smoyer J L, English T S, Norris P M, Beechem T E and Stewart D A 2010 Ultrafast thermoelectric properties of gold under conditions of strong electron–phonon nonequilibrium *J. Appl. Phys.* **108** 104907

[32] Jackson J D 1999 *Classical Electrodynamics* (New York: Wiley)

[33] Petrovykh D Y, Altmann K N, Höchst H, Laubscher M, Maat S, Mankey G J and Himpsel F J 1998 Spin-dependent band structure, Fermi surface and carrier lifetime of permalloy *Appl. Phys. Lett.* **73** 3459–61